DISCLOSE the Neurodegeneration Dynamics: Individualized ODE Discovery for Alzheimer's Disease Precision Medicine

Wooseok Jung*[1,2], Joonhyuk Park*[3], and Won Hwa Kim[3]

[1] VUNO Inc., Seoul, South Korea
https://vuno.co/en/
[2] UC Berkeley-UCSF Graduate Program in Bioengineering, Berkeley, CA
Wooseok.Jung@ucsf.edu
[3] Pohang University of Science and Technology, Pohang, South Korea
{pjh1023,wonhwa}@postech.ac.kr

Abstract. Monitoring progression from Mild Cognitive Impairment due to Alzheimer's Disease (MCI-AD) is critical for patient care. However, current approaches to model AD progression overlook complex interrelated neurodegeneration in different regions of the brain and how AD pathology and genotypes manipulate it. This study defines neurodegeneration dynamics and proposes the Dynamics Individualized by Static Covariates without LOngitudinal ScrEening (DISCLOSE) framework. This method predicts individualized neurodegeneration dynamics from only baseline amyloid-beta deposition and the number of APOE4 alleles with an Ordinal Differential Equation (ODE). We evaluated DISCLOSE using longitudinal MRI samples in the Alzheimer's Disease Neuroimaging Initiative (ADNI) cohort. The results demonstrate that DISCLOSE outperforms existing methods in long-term trajectory prediction, particularly for predictions beyond three years. This work presents a significant step toward modeling individualized disease trajectories. Also, DISCLOSE could quantitatively interpret the effects of AD-related genotypes and pathophysiology on regional atrophy progression.

Keywords: ODE · Alzheimer's disease · Neurodegeneration Dynamics.

1 Introduction

Alzheimer's disease (AD), the most prevalent form of dementia, is now understood as a continuum that spans a preclinical stage of AD with underlying pathophysiological developments to stages of severe cognitive decline [2]. Mild cognitive impairment (MCI) due to AD (MCI-AD), representing an early stage in the continuum, is characterized by cognitive deficits that do not significantly affect daily life [10]. Approximately 30% to 50% of individuals with MCI-AD progress to Alzheimer's dementia within a decade [16], which emphasizes the importance of identifying MCI patients who are more likely to be exacerbated.

* Wooseok Jung and Joonhyuk Park contributed equally to this paper.

Amyloid beta ($A\beta$) protein accumulation in the brain is a key pathological hallmark of AD, forming insoluble plaques that disrupt neuronal function [10]. Amyloid PET imaging is the gold standard measurement of $A\beta$ proteinopathy, which is typically expressed as standardized uptake value ratios (SUVRs) normalized to a reference region [11]. In addition, the Apolipoprotein E (APOE) genetic variant significantly increases an individual's risk of developing AD. In particular, the E4 homozygote is associated with earlier and more aggressive amyloid deposition than other alleles. Measurement of neurodegeneration resulting from AD pathology can be observed as brain atrophy on MRI scans. Starting from the medial temporal lobe and hippocampus, atrophy progresses to the cerebral cortex throughout the disease progression [4]. However, early diagnosis of AD solely based on the neurodegeneration biomarker is nonspecific [10]. Thus, to holistically diagnose and stage AD, the combination of amyloid PET measurement, APOE4 genotyping, and brain MRI analysis is essential.

Numerous studies have addressed the problem by predicting disease progression in MCI patients to dementia using machine learning. Several methods accompany brain MRI and amyloid or genotype information, and achieved high prediction performance (e.g., AUROC ≥ 0.85) [9]. However, how biological changes lead to local or global neurodegeneration has not been precisely modeled. Also, how the atrophies of multiple brain regions are intercorrelated during the AD continuum is usually overlooked.

Contributions. The AD continuum can be viewed as a dynamical system of neurodegeneration across multiple brain regions influenced by Aβ deposition and APOE4 alleles. We define it as the neurodegeneration dynamics. To model the dynamics, we propose *Dynamics Individualized by Static Covariates without LOngitudinal ScrEening* (DISCLOSE) framework. **1)** DISCLOSE generates an individualized Ordinary Differential Equation (ODE) from baseline information only, **2)** DISCLOSE outperforms other ODE discovery in neurodegeneration trajectory estimation. **3)** DISCLOSE could enhance the interpretability of neurodegeneration progressing during the AD continuum by identifying how AD-related genotypes and pathology influence region-specific neurodegeneration patterns beyond mere accuracy-focused conversion prediction. These insights offer practical values for clinical applications and understanding whole-brain level neurodegeneration during Alzheimer's continuum, which is important particularly in the era of recently approved anti-amyloid therapies [21,26].

1.1 Related Work

MCI to Dementia Conversion Prediction. Previous studies employ machine learning and deep learning methods to classify progressive MCI (pMCI) and static MCI (sMCI) subjects. These approaches typically compute gray and white matter volumes as well as cortical thickness from MRI scans, using these features as input for SVMs or extracting structural features directly from MRIs using a CNN-based encoder [9,28]. In addition to imaging-based methods, studies like [5] integrate non-imaging biomarkers, such as cerebrospinal fluid tests measuring amyloid burden, to enhance the classification performance. Moreover,

many studies highlight that the low baseline hippocampal volume and faster atrophy rate serve as key biomarkers for estimating the conversion [25].

Atrophy Quantification. Automated atlas-based voxel-based morphometry (VBM) software like FreeSurfer is widely used to quantify brain MRI in longitudinal analysis [8]. To improve computational efficiency and the generalizability of atlas-based methods, deep learning-based VBMs have been introduced in recent studies [23]. Some were commercialized and received regulatory approvals, available in clinical practice beyond research settings [12].

Individualized ODE Discovery. Individual subjects may exhibit distinct neurodegeneration patterns influenced by subject-specific covariates. This motivates the development of personalized dynamical models that can adapt to individual trajectories while preserving their relationship to population-level dynamics.

INSITE [14] framework discovers individualized ODEs in treatment effect monitoring. INSITE employs a two-stage process: 1) using the SINDy algorithm [5] to learn the population-wise ODE $\bar{F}$ from aggregate data, then 2) personalizing this base model through fine-tuning with individual trajectories and static covariates. This method demonstrates how population dynamics serve as a foundation for capturing patient-specific variations through sparse equation discovery. However, implementing such frameworks in clinical settings is limited. While population dynamics can be pre-computed and integrated into clinical software, the longitudinal data required to personalize the population dynamics is unavailable at a patient's initial visit, making immediate intervention infeasible.

2 Method

Let $\mathbf{x}_t^{(i)} \in \mathcal{D} \subseteq \mathbb{R}^{d_\mathcal{D}}$ and $\mathbf{v}^{(i)} \in \mathcal{V} \subseteq \mathbb{R}^{d_\mathcal{V}}$ be features and static covariates of a subject $i \in I = \{1, ..., N\}$ measured at time $t \in [0 : T]$, and $f^{(i)}$ denote an individualized dynamic of the subject i. Similar to INSITE [14], DISCLOSE initially predicts the population dynamics $\bar{f}$, which demonstrates the trajectory of $\mathbf{x}$ across all subjects. Afterward, DISCLOSE finds an optimal mapping A that maps $\mathbf{v}^{(i)}$ to an endomorphism $f^{(i)}$:

$$A : \mathcal{V} \to \mathcal{F}, \quad \mathcal{F} = End(\mathbb{R}^{d_\mathcal{D}}). \tag{1}$$

Hence, $f^{(i)} = A(\mathbf{v}^{(i)})$. To ensure the existence and uniqueness of the dynamics, $f^{(i)}$ should be continuous in t and Lipschitz continuous in $\mathcal{D}$, according to Picard's existence theorem [17]. For simplicity, we may let f be a linear function.

The key component of DISCLOSE is its unique loss function to optimize A:

$$L(\hat{\mathbf{x}}^{(i)}, \mathbf{x}^{(i)}, f^{(i)}, \bar{f}) = \|\hat{\mathbf{x}}^{(i)} - \mathbf{x}^{(i)}\|_1 + \lambda_1 \|f^{(i)} - \bar{f}\|_1 + \lambda_2 \|f^{(i)}\|_1, \tag{2}$$

where $\hat{\mathbf{x}}$ and $\mathbf{x}$ are the predicted (from $f^{(i)}$) and ground truth trajectories, respectively. The first term is the main reconstruction loss with ℓ_1-norm. The second term accounts for the dynamics difference, which prevents the predicted dynamics from deviating sharply from the population dynamics [14]. Also, the third term is LASSO regularization to make $f^{(i)}$ sparse. The overview of the DISCLOSE process is illustrated in Algorithm 1.

Algorithm 1 Dynamics Individualized by Static Covariates without Longitudinal Screening (DISCLOSE)

Input: Patient data $\mathcal{D}$; patient static covariates $\mathcal{V}$; deterministic ODE discovery method DE; DISCLOSE function A.
Output: Population dynamics $\bar{f}$; individualized dynamics $\{f^{(i)}\}_{i \in I}$
Start: $\bar{f} \leftarrow DE(\mathcal{D})$.
for $i = 1$ **in** $\mathcal{D}$ **do**
  $f^{(i)} = A(\mathbf{v}^{(i)})$
  Calculate DISCLOSE loss (Equation 2)
  backpropagate the loss to fit A
end for
repeat by *n_ epochs*

3 Modeling Neurodegeneration Dynamics

Assume that an ODE governs brain atrophy progression in the AD continuum:

$$\frac{d\mathbf{x}^{(i)}}{dt} = f(\mathbf{x}^{(i)}), \quad f(\cdot) \in \mathcal{F}(\mathbb{R}), \tag{3}$$

where $\mathbf{x}^{(i)} \in \mathbb{R}^{d_{\mathcal{D}}}$ represents the neurodegeneration of the i-th subject across $d_{\mathcal{D}}$ brain regions. While it can be defined as raw regional volume, a z-score or normative percentile, obtained by comparison with an age and sex-matched normal population, is generally preferred [18]. $\mathcal{F}(\mathbb{R})$ could be a real-valued function space, but for simplicity, let f be a linear transformation (i.e., a real-valued matrix). Then, $f_{j,k}$ encodes the coupling between region j and region k [13].

Covariates such as gender, genetic information, and structural connectivity could affect the neurodegenerative process. We assumed that the number of APOE4 alleles (ϵ) and amyloid burden (β) are significant factors in brain atrophy dynamics. Hence the equation (3) is modified as,

$$\frac{d\mathbf{x}^{(i)}}{dt} = f^{(i)}_{\epsilon^{(i)},\beta^{(i)}}(\mathbf{x}^{(i)}), \quad f^{(i)} \in M_{d_{\mathcal{D}}}(\mathbb{R}), \tag{4}$$

where $\epsilon^{(i)}$ and $\beta^{(i)}$ refer to the APOE4 and amyloid burden values of i-th subject.

3.1 Study Dataset

The study utilized 2,292 3T 3D T1-weighted volumetric brain MRI scans of 371 individuals with mild cognitive impairment (MCI) from the Alzheimer's Disease Neuroimaging Initiative (ADNI) database (`adni.loni.usc.edu`). All sampled subjects were followed up for at least three years. Following [3], subjects were labeled as pMCI (n = 63, Clinical Dementia Rating (CDR) global score increased from 0.5 to 1 within 3 yrs) or sMCI (n = 308, CDR remained 0.5).

Each subject comes with the number of APOE4 alleles and amyloid SUVR. The number of APOE4 alleles are encoded to $\epsilon \in E = \{0, 1, 2\}$ ($\epsilon = 0$: APOE4

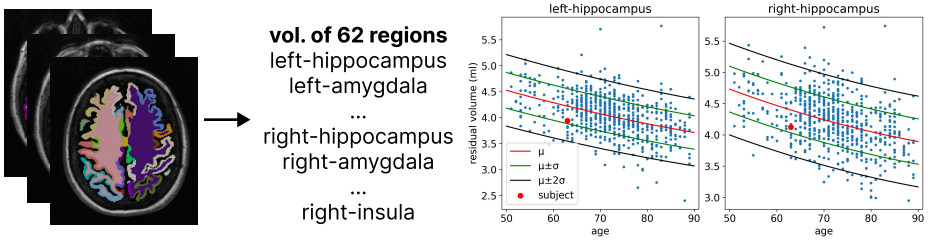

Fig. 1: Atrophy Quantification Pipeline. Left: whole brain segmentation to obtain volumes of 62 cortical and subcortical regions. Right: Calculate normative percentiles to rank the subject's regional bilateral hippocampal volumes against the cognitively normal population.

non-carrier, $\epsilon = 1$: APOE4 heterozygote, $\epsilon = 2$: APOE4 homozygote). We used the baseline global 18F-AV45 amyloid PET standardized uptake value ratio (SUVR) to encode amyloid burden β [11], which is typically within the range $[0, 2]$. The optimal cut-off for amyloid burden prediction is 1.11 [15].

3.2 Atrophy Quantification

Initially, we registered follow-up MRI scans to their corresponding baseline scans. Intracranial volume (ICV) and whole brain segmentation algorithms from VUNO Med-DeepBrain (DeepBrain) were employed to obtain volumes of 62 cortical and subcortical regions. DeepBrain has achieved dice score coefficient 0.82 in whole brain segmentation and 0.99 in ICV segmentation across multiple datasets [23,24]. It also showed high agreement with FreeSurfer [22]. To minimize volume changes due to head size differences, residual ICV adjustment was performed [27]. By comparing the volumes to an age- and sex-matched cognitively normal population, we derived the normative percentile (NP) values, representing the cumulative density of Gaussian random variables with a mean and variance estimated from the normative data (Figure 1). So, NP values are in the interval $[0, 1]$. Lower NP values indicate smaller volumes than the normal population, and therefore greater atrophy.

ADNI data have heterogeneous MRI acquisition time points. For instance, some have follow-ups after 3 or 6 months since baseline, while a few cases were tracked even after a decade. To cope with the data imputation issue, we fitted NP values of the j-th region to an exponential curve $x_j = a_j e^{-b_j t}$ $(0 < a < 1, b > 0)$, considering that they are strictly positive and will decrease. We sampled the data from $t = 0$ to $t = 5$ with the step size 0.25 to form our train and test data.

3.3 DISCLOSE for Modeling Neurodegeneration Dynamics

Given $\mathcal{D} = [0, 1]^{62}$, and $v = (\epsilon, \beta)$, i.e., a tuple of the number of APOE4 alleles and amyloid SUVR, we introduced an MLP to implement A that estimates f

from ϵ and β. A consists of two hidden layers containing 128 and 256 neurons with a dropout rate of 0.1, followed by LeakyReLU activation with $a = 0.1$ and batch normalization. The final layer returns a vector of dimension $3844 = 62^2$, then reshaped to a square matrix f. For the population dynamics $\bar{f}$, we used SINDy [5]. The dynamics tend to diverge if f is unbounded. Hence, we applied the $tanh(\cdot)$ to f at the end and divided it by 62, effectively making it stable.

4 Experimental Results

All models were trained and validated on one NVIDIA Tesla V100 GPU with CUDA 12.0. We used the ADAM optimizer ($\beta_1 = 0.9, \beta_2 = 0.999, \lambda = 1e-4, eps = 1e-5$). Considering the small values of predicted trajectories and therefore small gradients, the initial learning rate was set to 0.01, but we applied the ReducedOnPlateau learning rate scheduler (decay rate = 0.75, patience = 10). The batch size was set to 8, and we trained the model for 500 epochs, while the training stopped if the validation loss did not decrease for 50 epochs.

4.1 Comparison with Other ODE Discovery Methods

We evaluated the neurodegeneration trajectory estimation of DISCLOSE with ablation on loss terms in Equation (2). $\lambda_1 = 0.1$ and $\lambda_2 = 0.01$ uniformly, since we found the prediction accuracy does not substantially depend on choices of λ_1 and λ_2. Following [14], we assessed the root mean squared error (RMSE) between trajectories at each time point. We grouped time points before year one ($\tau < 1$), $\tau = 1, 2, 3$, and $\tau > 3$. We additionally measured matrix sparsity with threshold (SP_γ), the proportion of elements that are less than γ in absolute value relative to the total number of elements, and the mean absolute error (MAE) between predicted matrix and SINDy was scaled by 10^3.

We added two more baselines: 1) pure SINDy method without covariates (ϵ and β) (*SINDy*), and 2) the dynamics with diagonal A (*diagonal*). Hence, its ODE has the form $\dot{x_j} = g_j(\epsilon, \beta)x_j$, where $g : \mathbb{R}^2 \to \mathbb{R}^{62}$ is a linear function. Results for INSITE were omitted since applying SINDy twice (globally then individually) yielded unstable parameters in our task.

In Table 1, DISCLOSE methods outperformed SINDy, mainly when predicting the long-term after atrophy progression. SINDy showed almost no error (RMSE = 0.016) in predicting the atrophy within a year ($\tau < 1$), but the error consistently grows to 0.115 after three years and onward. This tendency was the same in the diagonal method, but the diagonal method exhibited inferior performance compared to SINDy. Both baseline covariates and interaction between brain regions seem necessary to accurately predict the dynamics.

On the other hand, DISCLOSE with different loss ablations showed similar RMSEs across the time points, while mostly achieving better RMSE than baseline methods. However, adding regularization to Equation (2) was not remarkably effective. The DISCLOSE loss only with the L1 trajectory distance term showed the best goodness-of-fit with ground truth trajectories at $\tau = 1$,

Table 1: Neurodegeneration prediction results. RMSEs between predicted and ground truth NP values of each time point are visualized. L1: L1 distance between trajectories, diff: dynamics difference, Lasso: Lasso regularization, SP_γ: sparsity with threshold γ, MAE: MAE between f and the SINDy matrix.

	L1	L1 + diff	L1 + diff + Lasso	SINDy [5]	diagonal
$\tau < 1$	$\mathbf{0.016 \pm 0.009}$	0.016 ± 0.009	0.018 ± 0.010	0.016 ± 0.008	0.018 ± 0.008
$\tau = 1$	$\mathbf{0.039 \pm 0.021}$	0.040 ± 0.022	0.045 ± 0.024	0.052 ± 0.024	0.057 ± 0.023
$\tau = 2$	$\mathbf{0.067 \pm 0.031}$	0.068 ± 0.033	0.078 ± 0.037	0.08 ± 0.03	0.087 ± 0.029
$\tau = 3$	$\mathbf{0.089 \pm 0.036}$	0.090 ± 0.039	0.104 ± 0.046	0.094 ± 0.031	0.102 ± 0.031
$\tau > 3$	$\mathbf{0.108 \pm 0.040}$	0.108 ± 0.043	0.127 ± 0.053	0.115 ± 0.033	0.125 ± 0.035
SP_γ	0.006 ± 0.002	0.006 ± 0.002	0.04 ± 0.049	**0.668**	N/A
MAE	5.232 ± 0.122	5.229 ± 0.143	$\mathbf{5.145 \pm 0.167}$	N/A	N/A

$\tau = 1$, and $\tau > 3$. Adding dynamics difference regularization showed the highest performance at $\tau = 2$ and $\tau = 3$. This consistency across different time points suggests that the DISCLOSE framework is more robust to temporal variations in neurodegeneration patterns than baseline approaches, potentially making it more reliable for clinical applications where prediction stability is crucial. Still, the differences between RMSEs were small. MAE slightly decreased, and these methods failed to generate sparse dynamics. The Lasso regularization term did not improve the trajectory estimation accuracy, but the sparsity marginally rose to 0.04, yet substantially less than that of SINDy (i.e., 0.668).

4.2 Interpretable Dementia Conversion Prediction

Using $f^{(i)}$s obtained from Equation (4), we examined regional correlations across different APOE4 genotypes ϵ and amyloid burden SUVRs β. Table 2 and Figure 2 present the averaged prediction f of n subjects for each category of ϵ and β.

Interestingly, dynamical patterns substantially aligned with previous neuroimaging studies on AD patients. A clear trend emerges when comparing connectivity within the same APOE4 group. Individuals with elevated amyloid ($\beta > 1.11$) exhibit stronger coupling than their lower amyloid ($\beta \leq 1.11$) counterparts across all APOE4 groups. Similarly, the coupling tends to increase as the number of APOE4 alleles rises (i.e., $\epsilon = 0, 1, 2$), reinforcing the known genetic influence of APOE4 on Alzheimer's disease (AD) pathology [1]. Additionally, the entorhinal cortex and amygdala remain consistently connected across all conditions, with coupling localized to regions within the medial temporal lobe (dark gray in Table 2) [7]. These observations align with established neurodegenerative patterns in AD, as the medial temporal lobe is known to show atrophy associated with disease progression in the early stages [4]. In the highest-risk group (top right in Table 2), temporal lobe atrophy diffuses from medial to lateral regions such as the fusiform and middle temporal gyri, similar to typical neurodegeneration progression in AD [10].

Table 2: Top 5 connectomes of the averaged predicted fs w.r.t. amyloid burden β and the number of APOE4 alleles ϵ. w is the edge weights scaled by 10^{-3}.

Amyloid (β)	APOE4 non-carrier ($\epsilon = 0$)			APOE4 heterozygote ($\epsilon = 1$)			APOE4 homozygote ($\epsilon = 2$)		
	w	ROI	ROI	w	ROI	ROI	w	ROI	ROI
High ($\beta > 1.11$)	3.89	L-entorhinal	L-amygdala	4.37	L-entorhinal	L-amygdala	5.01	R-fusiform	L-mid_temp
	3.41	L-inf_temp	R-sup_front	3.94	L-thalamus	L-sup_front	4.95	L-entorhinal	L-amygdala
	3.34	L-inf_temp	L-sup_front	3.92	L-inf_temp	R-sup_front	4.80	L-thalamus	L-sup_front
	3.21	L-thalamus	L-sup_front	3.85	R-fusiform	L-min_temp	4.60	R-insula	R-amygdala
	3.18	R-precuneus	R-sup_temp	3.84	L-inf_temp	L-sup_front	4.51	L-inf_temp	R-sup_front
Low ($\beta \leq 1.11$)	3.09	L-entorhinal	L-amygdala	3.10	L-entorhinal	L-amygdala	3.22	L-entorhinal	L-amygdala
	2.79	R-inf_pari	L-fusiform	2.82	R-inf_pari	L-fusiform	2.91	L-insula	L-amygdala
	2.67	R-precuneus	R-sup_temp	2.81	R-med_occ	R-amygdala	2.89	R-med_occ	R-amygdala
	2.66	R-med_occ	R-amygdala	2.69	L-insula	L-amygdala	2.88	R-inf_pari	L-fusiform
	2.64	L-inf_pari	R-para_hip	2.62	L-inf_temp	L-sup_front	2.76	L-inf_temp	L-sup_front

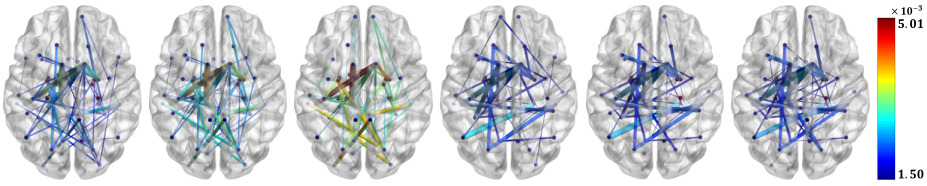

(a) (b) (c) (d) (e) (f)

Fig. 2: The averaged predicted f across n subjects in each group: ($\epsilon = 0$, high $\beta, n = 66$), ($\epsilon = 1$, high $\beta, n = 101$), ($\epsilon = 2$, high $\beta, n = 28$), ($\epsilon = 0$, low $\beta, n = 133$), ($\epsilon = 1$, low $\beta, n = 36$), and ($\epsilon = 2$, low $\beta, n = 6$), corresponding to (a)-(f), respectively. Colors and thickness of the edges represent the edge weights.

Low amyloid ($\beta \leq 1.11$) groups exhibit notable influence from the parietal and occipital regions, unlike the high amyloid groups (light gray in Table. 2). Those atypical AD cases often exhibit pronounced posterior atrophy, particularly in the medial parietal regions, advocating our findings [20].

5 Conclusion

We proposed the neurodegeneration dynamics showing the relationship among brain regions, which can estimate the onset of severe neurodegeneration. To predict the dynamics, we introduced DISCLOSE, a framework that derives subject-specific dynamics of neurodegeneration using only baseline data and thereby aids longitudinal monitoring and simulation. Integrating APOE4 genotype and initial amyloid burden data, DISCLOSE significantly improved atrophy estimation while capturing the complex interactions between amyloid burden, APOE4 status, and progressive brain atrophy. We validated neurodegeneration dynamics both quantitatively and qualitatively. By understanding individual disease

progression patterns, this approach may fundamentally transform how we conceptualize, monitor, and ultimately treat neurodegenerative diseases.

Limitation. DISCLOSE comes with limitations. It lacks sparsity and is not suitable for handling data variability. As a future work, adding explicit regularization for sparsity can be considered, as well as stochastic differential equations to effectively capture data variability. While we used MLPs for the dynamics matrix, sparse graph neural networks could potentially enhance spatial relationship modeling [6,19]. Finally, our validation was limited to a single cohort, which can be extended in a longer version of our work.

Acknowledgments. W. Jung was employed at VUNO Inc. while completing this work. Data collection and sharing for this project were funded by the Alzheimer's Disease Neuroimaging Initiative (ADNI) (National Institutes of Health Grant U01 AG024904), DOD ADNI (Department of Defense award number W81XWH-12-2-0012), and AI Graduate Program at POSTECH (RS-2019-II191906).

Disclosure of Interests. The authors have no competing interests to declare that are relevant to the content of this article.

References

1. Agosta, F., Vossel, K.A., et al.: Apolipoprotein e $\varepsilon 4$ is associated with disease-specific effects on brain atrophy in alzheimer's disease and frontotemporal dementia. Proceedings of the National Academy of Sciences **106**(6), 2018–2022 (2009)
2. Aisen, P.S., Cummings, J., et al.: On the path to 2025: understanding the alzheimer's disease continuum. Alzheimer's research & therapy **9**, 1–10 (2017)
3. Albert, M.S., DeKosky, S.T., et al.: The diagnosis of mild cognitive impairment due to alzheimer's disease: recommendations from the national institute on aging-alzheimer's association workgroups on diagnostic guidelines for alzheimer's disease. Focus **11**(1), 96–106 (2013)
4. Barkhof, F., van Buchem, M.A.: Neuroimaging in dementia. Springer (2016)
5. Brunton, S.L., Proctor, J.L., et al.: Discovering governing equations from data by sparse identification of nonlinear dynamical systems. Proceedings of the national academy of sciences **113**(15), 3932–3937 (2016)
6. Cho, H., Sim, J., et al.: Neurodegenerative brain network classification via adaptive diffusion with temporal regularization. In: Forty-first International Conference On Machine Learning (2024)
7. Enkirch, S.J., Traschütz, A., et al.: The erica score: an mr imaging–based visual scoring system for the assessment of entorhinal cortex atrophy in alzheimer disease. Radiology **288**(1), 226–333 (2018)
8. Fischl, B.: Freesurfer. Neuroimage **62**(2), 774–781 (2012)
9. Grueso, S., Viejo-Sobera, R.: Machine learning methods for predicting progression from mild cognitive impairment to alzheimer's disease dementia: a systematic review. Alzheimer's research & therapy **13**, 1–29 (2021)
10. Jack Jr, C.R., Andrews, J.S., et al.: Revised criteria for diagnosis and staging of alzheimer's disease: Alzheimer's association workgroup. Alzheimer's & Dementia **20**(8), 5143–5169 (2024)

11. Jagust, W.J., Bandy, D., et al.: The alzheimer's disease neuroimaging initiative positron emission tomography core. Alzheimer's & Dementia **6**(3), 221–229 (2010)
12. Jeong, S.Y., Suh, C.H., et al.: Brain mri-based artificial intelligence software in patients with neurodegenerative diseases: current status. Journal of the Korean Society of Radiology **83**(3), 473–485 (2022)
13. Jung, W., Kim, S., et al.: Modelling brain atrophy dynamics enhances predicting cognitive decline in alzheimer's disease continuum. In: Cognitive Computational Neuroscience (2024)
14. Kacprzyk, K., Holt, S., et al.: Ode discovery for longitudinal heterogeneous treatment effects inference. arXiv preprint arXiv:2403.10766 (2024)
15. Landau, S.M., Lu, M., et al.: Comparing positron emission tomography imaging and cerebrospinal fluid measurements of β-amyloid. Annals of neurology **74**(6), 826–836 (2013)
16. Liss, J., Seleri Assunção, S., et al.: Practical recommendations for timely, accurate diagnosis of symptomatic alzheimer's disease (mci and dementia) in primary care: a review and synthesis. Journal of internal medicine **290**(2), 310–334 (2021)
17. Murray, F.J., Miller, K.S.: Existence theorems for ordinary differential equations. Courier Corporation (2013)
18. Orellana, C., Ferreira, D., et al.: Measuring global brain atrophy with the brain volume/cerebrospinal fluid index: normative values, cut-offs and clinical associations. Neurodegenerative Diseases **16**(1-2), 77–86 (2016)
19. Park, J., Hwang, Y., et al.: Convolving directed graph edges via hodge laplacian for brain network analysis. In: International Conference on Medical Image Computing and Computer-Assisted Intervention. pp. 789–799. Springer (2023)
20. Ross, S., Graham, N., et al.: Progressive biparietal atrophy: an atypical presentation of alzheimer's disease. Journal of Neurology, Neurosurgery & Psychiatry **61**(4), 388–395 (1996)
21. Sims, J.R., Zimmer, J.A., et al.: Donanemab in early symptomatic alzheimer disease: the trailblazer-alz 2 randomized clinical trial. Jama **330**(6), 512–527 (2023)
22. Song, H., Lee, S.A., Jo, S.W., et al.: Agreement and reliability between clinically available software programs in measuring volumes and normative percentiles of segmented brain regions. Korean Journal of Radiology **23**(10), 959 (2022)
23. Suh, C., Shim, W., et al.: Development and validation of a deep learning–based automatic brain segmentation and classification algorithm for alzheimer disease using 3d t1-weighted volumetric images. American Journal of Neuroradiology **41**(12), 2227–2234 (2020)
24. Suh, P.S., Jung, W., et al.: Development and validation of a deep learning-based automatic segmentation model for assessing intracranial volume: comparison with neuroquant, freesurfer, and synthseg. Frontiers in Neurology **14**, 1221892 (2023)
25. Tabatabaei-Jafari, H., Shaw, M.E., et al.: Regional brain atrophy predicts time to conversion to alzheimer's disease, dependent on baseline volume. Neurobiology of aging **83**, 86–94 (2019)
26. Van Dyck, C.H., Swanson, C.J., et al.: Lecanemab in early alzheimer's disease. New England Journal of Medicine **388**(1), 9–21 (2023)
27. Voevodskaya, O., Simmons, A., et al.: The effects of intracranial volume adjustment approaches on multiple regional mri volumes in healthy aging and alzheimer's disease. Frontiers in aging neuroscience **6**, 264 (2014)
28. Xu, L., Yao, Z., et al.: Sparse feature learning with label information for alzheimer's disease classification based on magnetic resonance imaging. IEEE Access **7**, 26157–26167 (2019)